JATIS Journal of Astronomical Telescopes, Instruments, and Systems

RESEARCH PAPER

On the effects of spider-arms vignetting on interferometric measurements of deformable mirrors

Runa Briguglio,[a],* **Giorgio Pariani**,[b] **Marco Xompero**,[a] **Nicolò Azzaroli**,[a]
Chiara Selmi,[a] **Armando Riccardi**,[a] **and Luca Oggioni**[b]
[a]INAF Osservatorio Astrofisico Arcetri, Firenze, Italy
[b]INAF Osservatorio Astronomico di Merate, Lecco, Italy

ABSTRACT. The interferometric calibration and measurement of deformable mirrors for adaptive optics are often performed on complex optical system with spider arms. The spider shadows may divide the mirror surface into separate islands on the detector, so the interferometer fails in reconnecting them to a common phase value. The calibration measurements then suffer from such artificial differential pistons across islands, which is converted into a wrong actuator command and in general into a poor calibration. We review the effects of spider arms shadowing as experienced during the optical calibration of large format adaptive mirrors, such as the Large Binocular Telescope and Very Large Telescope ones; we describe the procedures that we tested to cope with these issues and their effectiveness; and we present a laboratory assessment of the effect of such a shadowing with a dedicated test setup. Our work is part of a preparatory activity for the optical test of the European Extremely Large Telescope adaptive mirror M4.

[DOI: 10.1117/1.JATIS.9.2.029002]

Keywords: adaptive optics; wavefront correctors; deformable mirrors; optical calibration; spider

Paper 22098G received Oct. 13, 2022; revised May 11, 2023; accepted May 12, 2023; published Jun. 2, 2023.

1 Introduction

Spider arms are commonly used in telescopes and other optical systems to hold mirrors and instruments within the beam. In an optical telescope, for instance, a spider arm is used to suspend the secondary mirror on the optical axis at the proper distance from the primary mirror. The effects of the spider shadowing are well known[1] in terms of resulting point spread function (PSF) and contrast loss; this is the reason why a big effort has been made in the modeling and designing of spider arm structures with a minimal impact on the PSF.

Within this work, we discuss a less familiar effect. We consider the case of a deformable mirror (DM) with a wavefront (WF) image (as measured by an interferometer or a WF sensor) that is divided into islands by the spider shadows; in particular, we consider a continuous, i.e., not segmented, DM. Many wavefront sensor (WFS) are not sensitive to the absolute piston signal; an interferometer, for instance, is able to retrieve surface maps modulo lambda only. When dealing with non continuous images, the reconstruction algorithm fails the identification of the real vertical distance among the islands and assigns them a $n\lambda$ value, with arbitrary n. This is particularly concerning during astronomical observations when the DM is controlled in a closed loop by the

---

*Address all correspondence to Runa Briguglio, runa.briguglio@inaf.it

WFS. In the context of the adaptive telescopes, many groups are working to cope with such an issue; see for instance other studies.[2–5]

In general, it is possible to reconnect in phase (or bridging) the WF measurement of a contiguous, rigid mirror separated into islands due to the continuity of the mechanical surface. Some advanced interferometer software offers such utility (known as island leveling); the user may choose among various algorithms, such as joining the gap or making co-planar, depending on the optical surface under test. Also in post-processing, some assumptions on the known mirror shape may help. For instance, one may subtract from the mirror WF image a given aberration approximating the mirror shape or the current alignment; once an almost flat residue is obtained, it is then possible to adjust the differential piston on the islands to the same value, or at least to reduce it within an acceptable threshold. Let us mention here the difference between bridging and phasing. The former is the correction of a WF image with a non-existent vertical step on a mechanically continuous surface, produced by a sensor due to missing or poor information; phasing is the measurement and correction of the real phase step between two physically separated optical areas.

Things are much different for a DM, with a surface shape that is changed any time with the actuators command applied. A DM is in fact calibrated with the optical feedback of the interferometer; if the surface image is divided into separated islands, each with a different measured piston value, the calibration fails.

During the measurement of the actuator or mirror mode influence functions (IFs), the wrong piston values on the islands are spread across all measurements forming the system optical interaction matrix, which is in turn blended at the spatial scale of the islands. The effect is even worse during the mirror flattening (which is the computation of the actuator command to produce a minimum WFE); in fact, to compensate for the piston signal on the islands, the actuators push or pull the mirror optical surface accordingly and produces a sharp kink corresponding to the spider shadow. As the bent area is vignetted, post-facto bridging strategies may be not available.

Another crucial point is that the actuators below the shadow have no interferometer or WFS feedback and cannot be optically calibrated or operated in an optical close loop. Depending on the actuator's working principle (e.g., piezo, voice coil with internal metrology), a dedicated control strategy will be identified and implemented.

A robust and effective solution is to keep the spider shadow as small as possible (e.g., smaller than the interferometer resolution element) and avoid any obscuration, at the cost of a lower system stiffness and possibly a larger impact of vibration noise. Such by design approach shall be validated, at least to assess statistically the occurrence of spider-related reconstruction errors.

The aim of the paper is to investigate experimentally the conditions responsible for the occurrence of island errors and in general of reconstruction errors related to the spider shadow. The ultimate goal is to draw some design and measurement guidelines to reduce the probability of errors to a minimum. The context of this work is related to our experience with the interferometric measurements of large format DMs and to the future optical calibration of the European Extremely Large Telescope (E-ELT) adaptive mirror M4. In the following, we compare the cases of the interferometric measurement of the Large Binocular Telescope (LBT) and Magellan Telescope adaptive secondaries (in Sec. 2.1) with the Very Large Telescope [VLT; unit telescope-4 (UT4)] one (in Sec. 2.2), all of them subjected to long calibration campaigns on their optical test-benches and at the telescope. The different spider-arms allow us to draw some qualitative considerations about their shadowing in two extremal conditions, presented in Sec. 3. We then present (see Sec. 2.3) the case of the forth-coming calibration of the ELT adaptive mirror M4 on its optical facility.

After such a preliminary survey, we present in Sec. 4 a laboratory campaign on a dedicated test-bed reproducing the M4 one; the goal of such tests is to investigate statistically the occurrence of spider-related errors, depending on spider thickness, local slope, and reconstruction parameters. We summarize the laboratory results into lessons learned and a laboratory procedure to minimize the probability of errors.

In Appendix B, we briefly discuss some of the processing algorithms the we developed to tackle with spider-arms vignetting problems during the optical tests on the VLT-deformable secondary mirror (DSM) to include two bridging algorithms, for both absolute and differential sampling, and a procedure for the control of masked actuators.

2 Context: Interferometer Calibration of Large Format DMs

2.1 LBT and Magellan DMs

The LBT adaptive secondaries[6] are 911 mm diameter concave elliptical mirrors, controlled by 672 actuators. The Magellan mirror[7] is basically the clone of the LBT ones, with a slightly lower diameter (850 mm) and 585 actuators. We present our results obtained during the calibration campaign[8,9] on the three systems together. Given the optical prescription, the DM is measured with the interferometer located at the ellipse long focus and a retro-reflector (RR) at the short one. The RR optics is held by 4 blades 2.5 mm thick. Such dimension will be compared with a pixel scale of 1.8 mm/pixel (corresponding to 3.6 mm/metapixel, i.e., the resolution element where the phase is computed; see Sec. 3 for a definition of metapixel). We note that the blades are placed at ∼45 deg with respect to the pixel grid; due to this diagonal arrangement, the shadow thickness is actually fully contained within a single metapixel. The effect of this occurrence is discussed in Sec. 3. A typical phase map of the LBT DM is shown in Fig. 1. The points belonging to the vignetted area are reconstructed by the software (SW) with random values (when compared with the neighboring); the values are in the range of $-150\ \text{nm} \approx 80\ \text{nm}$, with an extension that is smaller than $\lambda/2$. The mirror phase map is continuous across the spiders, and this point has been verified in many years of measurements; on a sample larger than $5 \cdot 10^5$ collected frames, the incidence of phase maps with islands reconstruction errors is limited to a few cases, all of them related to very marginal working conditions (e.g., extremely poor alignment, heavy vibrations). Compared with the actuator pitch on the detector (34 pixel/actuator), the obstruction is negligible and no actuator suffered from signal loss because of the spider.

2.2 VLT Case

The VLT-UT4 adaptive secondary [also known as deformable secondary mirror (DSM)] is 1.2 m in diameter and controlled by 1170 actuators. The working principle and technology is the same as the LBT adaptive secondary mirror (ASM). The mirror has been calibrated[10] on a dedicated test facility called Adaptive Secondary Setup and Instrument STimulator (ASSIST),[11] located at the European Southern Observatory (ESO) Headquarters in Garching (Germany). The pixel-scale on ASSIST is 1.2 mm/pixel (corresponding to 2.4 mm/metapixel), and the test optics are held by two sets of thick blades, requested to simulate on the test-bench the obstruction of the VLT-UT4 spider structure. In addition, the two sets are not perfectly superimposed, so in the end the effective obscuration is 32 mm projected on the DSM, corresponding to 26 pixels. The impact on the interferometric images was very heavy: we estimated that more than 70% of the images collected ($\approx 2 \cdot 10^5$ during the entire test run) was affected by island errors. In Fig. 2, we show the fringe image of the DSM after the flattening procedure to present the effects

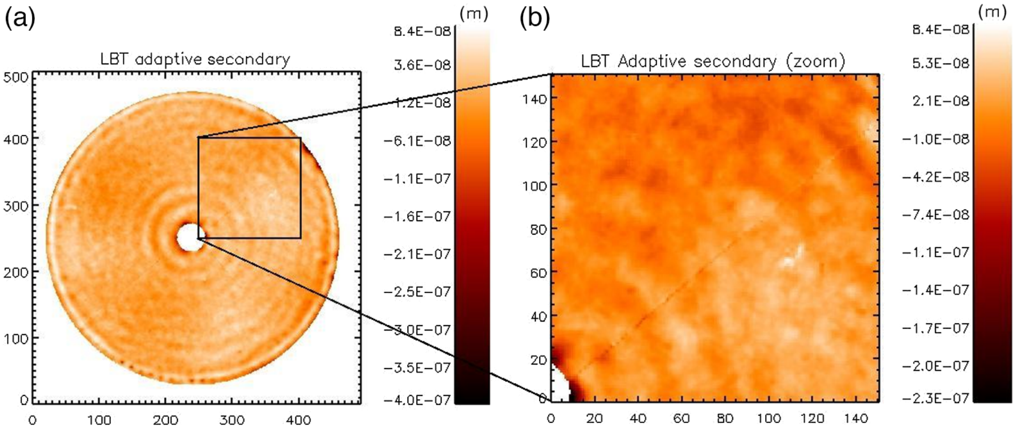

Fig. 1 (a) Surface map of the LBT ASM, (b) with a close-up of the spider shadow. The pixels below the spider are wrongly reconstructed, i.e., their values are random within the interferometer range.

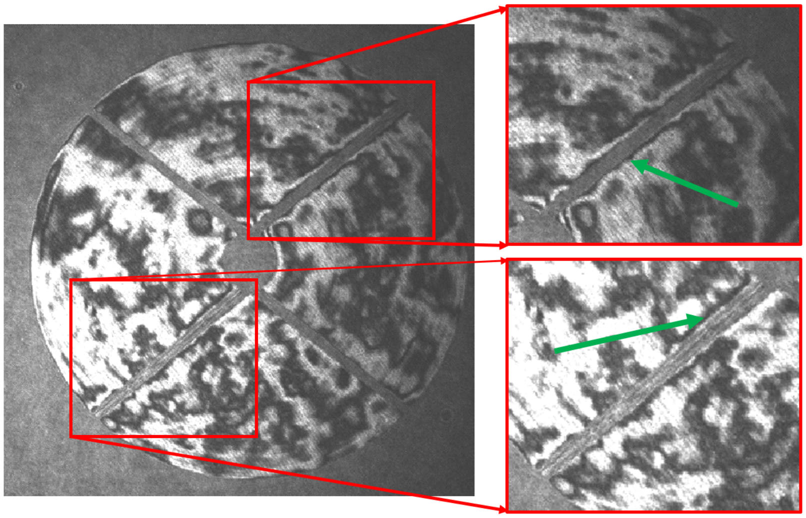

Fig. 2 Interferogram of the VLT-DSM, to show the shadow due to the thick spider. The black fringe (green arrows) just below the top-right and bottom-left spider indicates a kink in the optical surface parallel to the spider and is due to a (wrong) DM command to compensate for an island error during the calibration process. For comparison, the fringe is not observed in the corresponding top-left and bottom-right spider.

of the island error on the DSM. It is possible to notice a sharp fringe below the blades as indicated in the figure: the islands of the DM have been differentially pushed by the actuators to compensate for the (artificial) differential piston read by the interferometer.

During the laboratory activity on ASSIST, we implemented and tested some island leveling techniques, and we give a quick summary of them in Appendix B. In summary, the results were in the end positive only for the differential samplings, i.e., the measurements of the actuators IF (more details in Sec. 7.3). For the cases of absolute measurements (i.e., those to sample the current DM shape, as requested for the flattening procedure), the results were substantially poor. The final delivered flattening command was visually inspected from the fringes image to check for the presence of differential piston commands applied by the actuators.

The actuator pitch on the detector is 25 pixel/actuator; because the effective obscuration by the spider is 20 pixel, we were forced to implement a dedicated control strategy for those actuators heavily masked out. A summary on the actuators selection and control strategy is presented in Sec. 7.4.

2.3 Toward the E-ELT Adaptive Mirror M4

The adaptive M4 unit (M4), the ground-layer WF corrector of the E-ELT, will be the largest DM equipping an astronomical adaptive optics (AO) system. M4 is a 2.4 m flat DM shaped by 5316 voice-coil actuators. The mirror is composed of six mechanically separated segments or petals, each controlled independently from the others.

The M4 DM will be optically measured on an optical test tower (OTT[12]). Because a full aperture test would involve an incredibly large test equipment, a macro-stitching approach will be followed. The OTT will provide a 1.5 m collimated beam, sliding below the mirror, large enough to image and calibrate the single shell. The beam may also look at the mirror center to remove the differential tip/tilt and piston between the segments. The collimated beam is produced by an on-axis parabolic mirror, $F/2.4$, fed by a relay system composed of three lenses and a folding mirror (a modified 4f design), mounted along with the interferometer on the same support. The lens and folding mirror are suspended above the center of the parabola by means of four spider-arms, vignetting the collimated beam, and are perfectly in focus at the interferometer camera because they are located near the M4 surface.

For an interferometer resolution of 1000×1000 pixel, the scale at the M4 level is 1.3 mm/pixel (or 2.6 mm/metapixel) and the as-designed spider thickness is 2.5 mm; with these parameters, the spider shadow corresponds to ~ 2 pixel (or 1 metapixel): the size and orientation were designed to be conservative to the conditions of the LBT and Magellan DMs and have been proven to be favorable. Nevertheless, we arranged a measurement campaign in the laboratory on a simplified optical setup, intended as a risk mitigation strategy for the OTT implementation. The goal is to cross-check the as-designed thickness of the spider and to identify the critical conditions of the test setup (alignment, local slope, and modulation threshold versus automatic trim of the edges).

Because of its segmented design, the M4 petals will be first individually flattened and then phased together to produce the final shape command. The phasing will be performed with a dedicated sensor to retrieve the real vertical distance between the segments. It follows that the spider shadow issue is particularly concerning for the case of M4 because we expect that managing both bridging and phasing will increase significantly the calibration complexity.

3 Interferometers and Spider Arms

3.1 Phase Reconstruction and Shadowing: A Working Model

In the previous sections, we compared the case of the optical measurements of the LBT and VLT adaptive secondaries, showing very different behaviors of the interferometer in the presence of spider due to different shadowing conditions. We now describe a possible working model involving spider thickness, geometry, shadowing, software parameters, and island errors. On the other hand, the source of these errors depends on the particular interferometer hardware and software considered. Software is generally proprietary, so it is not possible for the end-user to have a detailed view of the reconstruction algorithms and its behaviors in the presence of discontinuities; within the context of this work, we present a conceptual description of the interferometer that we used starting from the information in the literature. As first, let us recall a few well-known aspects.

1. An interferometer produces a WF map of the test by combining several measurements of the interference pattern, acquired with a known and fixed phase delay.
2. Because its working principle is the interference of light, it has an intrinsically local periodic response, i.e., the signal retrieved by its measurement element is in the range $[-\lambda/2;\lambda/2]$ (or equivalently $[0;\lambda]$), with λ being the working wavelength.
3. Such phase ambiguity implies that the largest local WF step across adjacent measurement elements shall be lower than λ.
4. The phase-unwrapping (or reconstruction) algorithm takes care of producing the final WF map by locally adding a $\pm\lambda$ offset, when requested, to obtain a continuous surface.
5. Finally, the modulation index [see Eq. (1)] is the amount of signal variation among the measurement elements associated with the fixed phase delays.

In our work, we used a PhaseCam-4020, which is a dynamic, Twyman-Green interferometer by 4D-Technology. Dynamic interferometry means that the WF map is measured after a single exposure; conversely, traditional phase shifting interferometers need to collect four or more time-separated frames, and the delay is added mechanically. Dynamic interferometry is implemented with different techniques, all of them based on the contemporaneous imaging of the test with the different delays. Common techniques are the spatial carrier (a known tilt, e.g., a delay, added via a folding mirror), the use of multiple detectors (each with a known delay), and the pixelated phase-mask. A general review of the topic may be found in the literature, for instance in Refs. 13–15.

The pixelated phase-mask technique consists of a 2×2 pixel grid of fixed phase delays (0 deg, 90 deg, 180 deg, 270 deg) attached to the detector. A single raw frame may therefore be split into four images corresponding to the traditional four phase-shifted signals. With the four buckets algorithm, four neighboring pixels are combined to produce a single resolution element in the final phase map; alternatively, they can be combined with a windowed convolution-like algorithm to obtain a frame with almost the same resolution of the detector. We refer to the 2×2 pixel block as a metapixel.

A possible arrangement of the phase delays with respect to the pixel grid is shown in Fig. 3, where the numbers inside each cell represent the delay, and the thicker grid marks the 2×2 pixels block or metapixel (the proposed arrangement is arbitrary and for clarification purpose only). Given a raw frame, the modulation index φ is computed for each metapixel (x, y), as

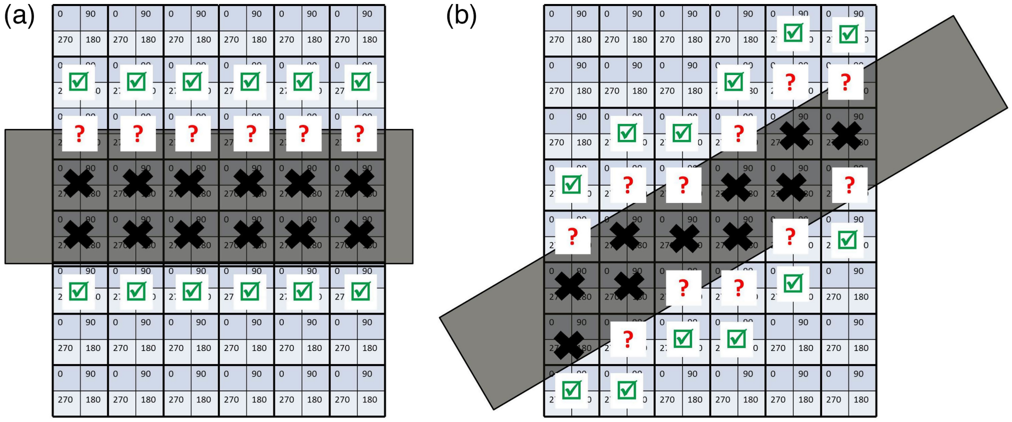

Fig. 3 Graphical representation of metapixel grid, shadow, and accepted/rejected pixels. Left panel: with spider parallel to pixel grid; right panel: with spider diagonal with respect to the pixel grid.

$$\varphi(x, y) = \frac{2\sqrt{(\alpha - \beta)^2 + (\gamma - \delta)^2}}{\alpha + \beta + \gamma + \delta}, \tag{1}$$

where the Greek letters indicate the intensity value registered on the four pixels belonging to the metapixel (x, y) [Eq. (4) of Ref. 13]. The modulation value is an indication of the amount of signal variation within the metapixel. If the modulation is $\frac{0}{0}$—this is the case of pixels outside the detector mask or below the spider shadow—the metapixel should be discarded from the phase retrieval computation. The user may select a minimum modulation threshold to automatically reject bad pixels or trim out the mask edges; a metapixel with insufficient modulation yields, in fact, reconstruction artifacts.

For a dynamic interferometer with pixelated phase mask, the reconstruction algorithm works under the assumption that the largest WF slope to be measured is $<\lambda/\text{metapixel}$; because the mirror under test is measured in reflection, its largest mechanical slope will then be $<\lambda/2/\text{metapixel}$ (we consider for simplicity an optical setup in which the mirror is measured in a single pass; in the following, we always refer to WF values). Intuitively, such a constraint on the local slope suggests that the WF step below the spider footprint is lower than λ.

We give a graphical representation of the behavior of the reconstruction algorithm in the presence of spiders in Fig. 3, where we show the vignetting projected by the spiders on the detector. Spiders are focused on the interferometer detector, as well as the mirror surface. As an example, we considered a 2.5 metapixel wide obscuration with horizontal and diagonal orientation with respect to the detector. We marked with a black cross the metapixels that are completely masked out, i.e., with $\varphi = 0$. We indicated with a red question mark the metapixels where the signal is not completely lost on at least 1 pixel out of 4; in this case, $\varphi \neq 0$ and the aperture is discarded only if φ is lower than the threshold defined by the user. Finally, we indicated with a green checkmark those metapixel close to the shadow with no or very marginal vignetting. A first observation is that, for a diagonal spider, a larger strip of poorly illuminated pixels may be expected; however, depending on the selected modulation threshold, the number of consecutive bad pixels may be larger or smaller.

Let us suppose that the reconstruction algorithm starts from the bottom-left pixel and moves vertically, column-wise, to the top of the frame. When a strip of discarded metapixels is encountered, they are skipped and the algorithm moves to the first valid pixel on the other island; then the raw phase value is computed, with the result being in the range of $-\lambda/2$ to $\lambda/2$; and finally, an offset is added, so the phase difference with respect to the last valid pixel before the strip is $<\lambda$, according to the assumption given before. If the real step is larger, the offset is not able to join the two islands and the retrieved phase will be discontinuous. We may then expect that the spider shadow reduces the local acceptable slope to λ/p, where p is the number of metapixels discarded along the processing direction.

Such a scheme fits well with our experience with DMs. In particular, in the case of the LBT DM, no island error was found, despite the vignetting being nominally 40% larger than the pixel size.

3.2 On the Effects of the Modulation Threshold

Let us consider another scenario in which the first valid metapixel has a low modulation index because of partial illumination on some of its pixels; the index is, however, larger than the user-selected threshold and the metapixel is accepted for reconstruction. The result may be affected by such poor modulation and be an artifact (as in Fig. 1), with a value very close to the edge of response range $\pm\lambda/2$. Now, depending on the local slope, the offset added to such a metapixel may be wrong because the artifact is interpreted as a real phase step. The wrong offset will be then propagated to the following metapixels, although they are now well illuminated. At this point, the phase error may affect only the column or the entire island, depending on the reconstruction algorithm and the values on the adjacent pixels.

This representation suggests that the modulation threshold may have a dramatic impact on the occurrence of island errors. Lowering the threshold results in a larger number of metapixel accepted; if the local slope is low, the artifacts due to poorly modulated metapixels are not enough to trigger an island error. A secondary benefit is that the clustering of rejected pixels causing holes in the mask is prevented; this is particularly important when combining a very large number of frames together. On the other hand, with a larger threshold, we expect a higher number of discarded metapixels, a larger gap below the spider, and consequently more errors with a given local slope.

In conclusion, we expect that the incidence of errors depends on a mix of parameters, such as obstruction size, current local slope, resolution, reconstruction algorithm, and user-defined parameters.

3.3 Qualitative Verification of the Working Model

The behavior presented above has been qualitatively checked in the laboratory, where we arranged an interferometric cavity with a resolution of 1.3 mm/pixel (see Sec. 4 for a complete description). We placed a 5 mm wide rod in front of the return mirror, masking three to four consecutive pixels on the detector, i.e., up to 2 metapixels. We computed the modulation index from a dataset, and it is presented in Fig. 4; the values across the shadow are spread in the range 0 to 0.2, whereas typical values on the surface are larger than 0.4.

We collected the WF map while changing the sampling parameters and the local slope and observed the following behaviors.

1. When the mirror is aligned within one to two fringes of WF tilt across the aperture, no island error is found.
2. With a low modulation threshold (e.g., 2%, 5%), the pixels below the spider are not masked but have almost random values.

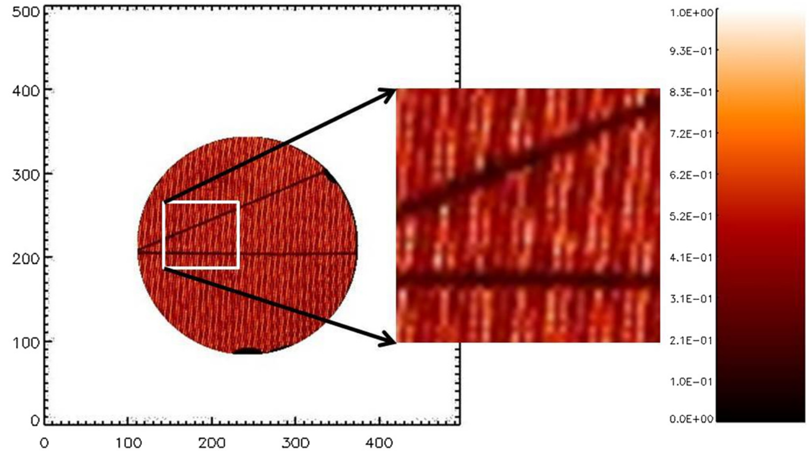

Fig. 4 Map of the modulation index, as measured during the laboratory testing.

3. In this condition, the WF map is continuous.
4. With a larger threshold (15%, 20%), many pixels below the spider are masked out but still a continuous WF map is obtained.
5. The number of island errors increases with the local slope; at the same time, a larger number of isolated reconstruction errors are detected.
6. When the fringes are vertical (i.e., the slope is negligible along the vertical axis), almost no errors are found, suggesting the idea of a vertical processing direction.
7. When the optical table is not floating (i.e., high frequency mechanical vibrations are not damped), the incidence of both island and local reconstruction errors is higher, even with a moderate tilt over the aperture.
8. When the spiders are masked by the user (with a proper detector mask), the phasemap is always divided into islands with different piston offsets, even in the presence of a negligible alignment tilt.

After such a preliminary test, we proceeded to a more robust and quantitative investigation.

4 Laboratory Assessment

4.1 Experimental Setup

We replicated the optical scheme of the OTT with a scaled, simplified version in our optical laboratory. We replaced the parabola and flat M4 mirror with a concave sphere illuminated from its center of curvature by a $F/2.4$ beam from the interferometer. The sphere is installed with its optical axis horizontal on the optical bench; the spider-arms are simulated by two aluminium rods placed at 3 cm from the sphere surface and installed on a metal frame. The first rod is horizontal, i.e., parallel to the pixel rows; the second is placed at an angle of 30 deg with respect to the pixel. The pixel scale is the same as in the OTT, and both the sphere and spider-arms are perfectly focused on the interferometer. Therefore, the setup implements the same imaging conditions for the spider-arms as in the OTT, allowing for a direct evaluation of their effects. In Fig. 5, we show the laboratory setup.

We prepared a set of rods with different thicknesses to produce a shadow on the sphere of 2 to 5 mm. Such values are to be compared with the nominal OTT full resolution pixel-scale of 1.3 mm/pixel (2.6 mm/metapixel, value to be doubled when working in low resolution).

The interferometer is the same dynamic, 4D-Technology Twyman-Green as described before. It is placed below the volume of the diverging beam, and a paper panel prevents the air flow from the ventilation slots from affecting the beam. The whole setup is installed on a pneumatic optical bench to reduce the vibrations.

The interferometer software allows for the fast collection of raw frames and post-processing at a later time. The post-processing, i.e., the phase-unwrapping, may be run several times on the same raw frame with different reconstruction parameters, such as a detector mask, filtering, data

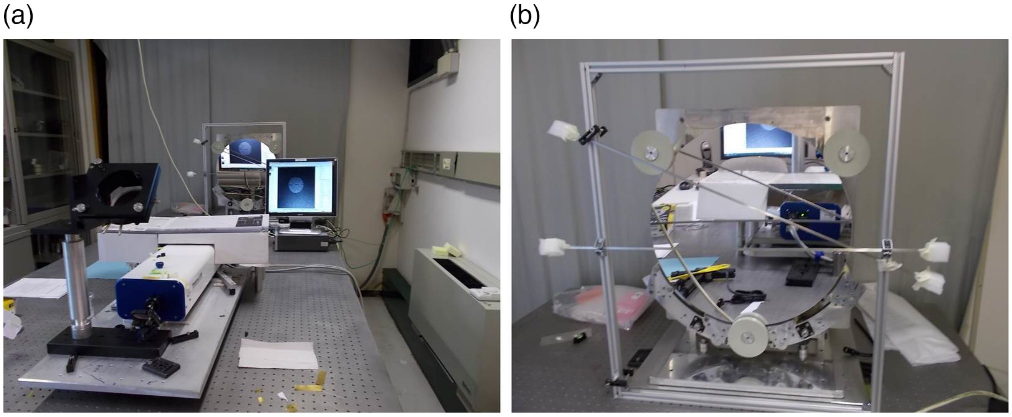

Fig. 5 (a) The optical setup in the laboratory, showing the optical bench and interferometer and (b) a close-up on the spherical mirror with the rods installed in front of the optical surface.

Table 1 Summary of slope and shadowing parameters.

Parameter	Value in low resolution	Value in high resolution
Pixel size	2.6 mm/pix	1.3 mm/pix
Metapix size	5.2 mm/mpix	2.6 mm/mpix
Metapix obscured, 2 mm rod	38%	—
Metapix obscured, 3 mm rod	57%	—
Metapix obscured, 4.2 mm rod	81%	162%
WF step across 1 metapix	310 nm	155 nm
WF step across 2 metapix	620 nm	310 nm

filling, and especially the modulation threshold. This feature is useful for testing the effect of the reconstruction parameters on the same raw data.

4.2 Data Collection

As a first step, we set all of the reconstruction parameters (except the modulation threshold) to a default value with the minimum impact on the reconstruction process: no data interpolation, no pixel trimming, and no filtering. We then modified sequentially the measurement setup to explore the entire parameters space, such as fringes density, fringes orientation, spider thickness, and modulation threshold. The spider orientation is tested automatically because we have two rods mounted with different angles with respect to the pixel direction.

We tested the high slope regime only because we already verified that no island errors are observed with a few fringes on the surface. Also, measurements at high fringes density are more conservative versus a real environment. In particular, we adjusted the setup to have a WF step similar to a critical $\lambda/2$ across the low resolution metapixel. We then had a typical WF peak-to-valley (PtV) across the 50 cm aperture of 30 μm, i.e., 60 nm/mm. The relevant test parameters are reported in Table 1. At each step, we collected a sequence of 1000 raw frames, and then we made several copies of the raw data and post-processed them with different modulation thresholds. In this way, we can directly compare the effect of the threshold on the very same raw data. For the case of 4.2 mm spider thickness, we also post-processed the raw frames at the interferometer full resolution.

4.3 Data Analysis Procedure

At the end of the phase-unwrapping, we analyzed each dataset of 1000 frames to count the island errors. The search is complicated by the large tilt in the frames, the many local reconstruction errors, and the large optical offset due to the 50 cm sphere; a procedure based on the computation of the local tilt and piston on each island to identify the phase steps is therefore not viable. In contrast, we adopted a data analysis based on the difference between consecutive frames, $dw = w_i - w_{i+1}$, where the cavity and the average alignment tilt are automatically nulled. A differential frame dw typically has a WF root mean square (RMS) of a few nanometers, and the identification of errors is straightforward. At first, we compared the WF RMS of each differential frame with a given reference threshold ($t_r = 20$ nm); when the WF is larger that the t_r threshold, we count a local reconstruction errors. Then, we created three regions of interest (ROIs) corresponding to the three islands; for each differential frame, we computed the mean value for each ROI and compared them with another reference threshold $t_p = 100\ \text{nm}(<\lambda)$. When the value is larger that t_p, we count an island error. Because we verified that the reconstruction algorithm moves vertically, bottom to top in the frame, the average in the lowest ROI never exceeds t_p; we then concluded that an island error in the second ROI is due to the horizontal spider (refer to Fig. 6), and an island error in the upper ROI is due to the diagonal spider. We could therefore identify separately the incidence of errors due to the two spiders.

In the end, we obtained for each dataset the percentage c_r of frames with local reconstruction errors and the percentage with island errors, separately due to the horizontal c_{ph} or the diagonal

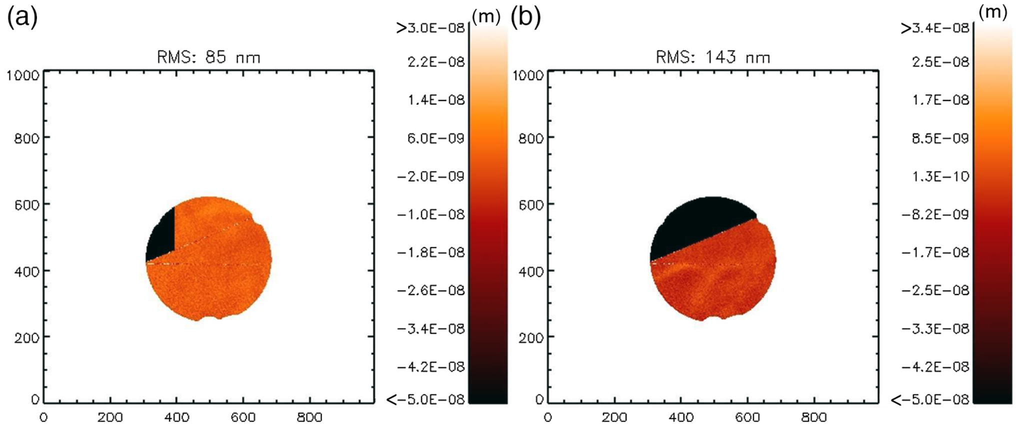

Fig. 6 (a) Sample of experimental data, showing a differential map with a local reconstruction error and (b) an island error due to the diagonal spider. Colorbars are limited to <30 nm; ≥50 nm to highlight the WF signal in the well-reconstructed area.

c_{pd} spider. Given the algorithm, the c_r count is taken as an upper limit because an island error will trigger the c_r counter as well.

The algorithm has an intrinsic weakness: if a pair of consecutive frames shows the same errors, the difference dw is not able to trigger any of the counter, thus leading to a underestimation of the errors. To prevent this occurrence, we verified on a sample that consecutive frames do not show identical island or reconstruction errors. This finding may be explained considering that reconstruction errors are triggered by the very local (spatial and temporal) conditions of the sampling, frame to frame, e.g., instantaneous convection and vibration, detector noise.

4.4 Results and Discussion

We summarized the percentage of island errors in Fig. 7, limited to the 4.2 mm test cases only, with a comparison of high resolution versus low resolution. The entire dataset is presented extensively in Table 2, for those readers interested in replicating the test or comparing their own findings.

No island errors were encountered testing the 2 and 3 mm thick spiders, whereas a major percentage of frames suffered from island errors in the 4.2 mm spider test; in this condition, no errors were detected with vertical tilt fringes and less than 10% errors with horizontal fringes and

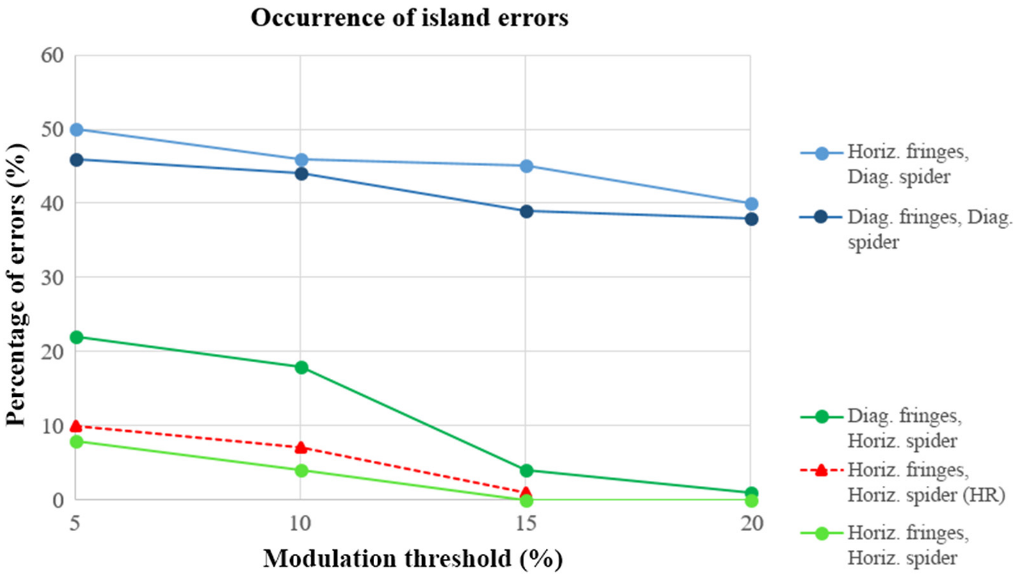

Fig. 7 Comparison between the occurrence of island errors for a subset of test conditions. Values in the *Y* axis are given as percentage of island errors detected in the dataset.

Table 2 Percentage of reconstruction c_r and island errors c_p in the datasets processed. For each fringes geometry, top and bottom rows for island errors are associated with diagonal c_{p_d} and horizontal spider c_{p_h}.

	Spider: 2 mm resolution: 500 × 500								Notes
Tilt fringes eom.	Reconstruction errors				Island piston errors				
Diag.	0	0	0.4	3.8	0	0	0	0	A0
					0	0	0	0	A1
Horiz.	0	0	0	0	0	0	0	0	A2
					0	0	0	0	A3
Vert.	0	0	0	0	0	0	0	0	A4
					0	0	0	0	A5
	Spider: 3 mm resolution: 500 × 500								
	Reconstruction errors				Island piston errors				
Diag.	6.4	0.2	0.2	29.6	0	0	0	0	B0
					0	0	0	0	B1
Horiz.	0.4	0	0	0	0	0	0	0	B2
					0	0	0	0	B3
Vert.	0	0	0	0	0	0	0	0	B4
					0	0	0	0	B5
	Spider: 4.2 mm resolution: 500 × 500								
	Reconstruction errors				Island piston errors				
Diag.	96	82.2	74.6	100	46.2	43.8	39.4	38.2	C0
					22.4	18.2	3.6	0.8	C1
Horiz.	93.2	85.2	59.4	64.8	50.4	45.8	44.6	40	C2
					8.4	4	0.4	0	C3
Vert.	2	0.4	0	0	0	0	0	0	C4
					0	0	0	0	C5
	Spider: 4.2 mm resolution: 1000 × 1000								
	Reconstruction errors				Island piston errors				
Diag.	0.6	0	0		0	0	0		D0
					0.6	0	0		D1
Horiz.	10.2	7	1.2		0	0	0		D2
					10.2	7	1.2		D3
Vert.	11.4	0.2	0		1.8	0	0		D4
					0.2	0	0		D5
Mod thresh (%)	5	10	15	20	5	10	15	20	

horizontal spider. For all cases, a lower occurrence of errors is observed with a large modulation threshold. The same 4.2 mm dataset, processed in high resolution, showed almost no errors, but for the case of horizontal fringes of tilt and horizontal spider, the errors incidence is similar in high resolution and in low resolution. Diagonal spider and fringe orientation yielded worse results in low resolution and better results in high resolution. The statistics of local reconstruction errors share the same behaviors: a higher incidence with low resolution, diagonal fringes of tilt, and lower modulation threshold.

To further discuss such behavior, we need to review the test parameters in Table 1. As mentioned, we adjusted the optical alignment to have 30 μm PtV over the 50 cm aperture, corresponding to a local slope of $\sim\lambda/2/$metapixel, in low resolution. Given the pixel scale, the 3 mm spider creates a shadow of 57% of a metapixel, spread on a single or more likely on two neighboring metapixels. In the case of a single obscured metapixel, even if rejected, the WF step of $\lambda/2$ below the shadow is within the interferometer acceptance range, and we expect no errors in this condition, as observed. When two neighboring metapixels are shadowed, the total step below the obscuration is λ, but because no errors are detected, we conclude that a (statistical) <30% vignetting per metapixel is not enough to trigger the rejection of both metapixel or produce artefacts, and in the end, this result in an island error. The same considerations apply for the case of the 2 mm thick spider.

Let us now focus on the 4.2 mm spider, corresponding to 81% of the metapixel size. The large error count indicates that the shadow is predominantly spread across two adjacent metapixel, and that they are not both discarded. In fact, the WF step below a single metapixel is within the interferometer range, so a single bad or rejected metapixel would not be enough to produce an error (probing the first statement), and the errors count is not 100% of the dataset (probing the second). We therefore have two metapixels in a row affected by poor signal (obscuration of up to 40% each), and we expect that such a condition could lead to a large fraction of reconstruction artefacts, i.e., random values of the reconstructed surface; see for e.g., Fig. 1. Because the total WF step is λ, those artefacts could result in island errors, as observed. We also notice that the modulation threshold plays a significant role in reducing the occurrence of errors. We guess that its effect is to discard the worst metapixel; if the following one is correctly reconstructed, no errors are expected because the total WF step is within the capture range. For higher threshold values, we expect that both metapixels are discarded and that 100% of the dataset suffers from island errors, as was demonstrated in Sec. 3.3, for a modulation threshold larger than 50%.

As a last point, we observe that the results in high resolution are way better than in low resolution, except for the case of horizontal spider and horizontal fringes of tilt. From Table 1, we find that the 4.2 mm spider shadows a 1.6 high resolution metapixel; we could then have two to three adjacent metapixels affected by low signal, with the central one being completely masked out. Given the local slope in high resolution, we have a total WF step of $\sim$465 nm; similar to our conclusions for the low resolution case, we argue that the artefacts due to poor signal are responsible for the island errors. Again, a correct modulation thresholding allows for discarding those bad pixel and a reconstruction of the WF map with significantly lower occurrence of island errors.

4.5 Lesson Learned

At the end of such testing session, we can draw some lessons learned for the optimization of the measurement setup.

1. Never mask the spider on the interferometer detector; if the software is instructed to skip the pixel below the spider, it will not even try to join the islands to the same WF level.
2. No errors are expected with a spider thinner than the resolution element.
3. Spider thickness should therefore be minimized to get minimal impact; however, the leading factor is the WF step across the shadow: a large spider could be accepted in very flat and quiet test-bed.
4. For a thin spider (compared to the pixel size), diagonal arrangements are preferable to prevent many adjacent pixels being affected by illumination issues.
5. Local reconstruction artefacts due to poor signal may be responsible for large error counts.
6. The rejection of a poorly illuminated pixel with a proper modulation threshold is the key to getting rid of artefacts.

7. On the other hand, an aggressive thresholding may result in large strips of discarded pixels and in turn in a large WF step across the edges of such strips, as well as more reconstruction errors. The modulation threshold should therefore be tuned on a trial-and-error basis.A more detailed procedure is given in Appendix A.

As a last point, we realized that, given the many actors and mutual interactions, a direct testing on the actual opto-mechanical setup is the key to finding the most suitable parameters and minimizing the interferometer errors. The reader may find in Appendix A some directions for inspecting the test setup and adjusting the modulation threshold.

5 Conclusions

The shadow of spider arms in interferometric measurement of DMs is responsible for high severity calibration issues, namely, a lack of optical feedback for some actuators and reconstruction artefacts, such as island errors, leading to poor mirror flattening commands. Such instances were observed on two very different cases, with the DM of the LBT and VLT, the opto-mechanical test setups of which have different spider arms.

In the frame of the preparatory activities for the optical calibration of the E-ELT DM M4, we arranged a test to quantitatively check the impact of such shadowing, to identify some laboratory guidelines and prevent the insurgence of these errors in other systems. We created the same optical layout of the M4 test-bench and tested a set of spider arms of variable thicknesses as long as the interferometer reconstruction parameters. We tested the system with the condition of a large tilt offset in the cavity, corresponding to half of the capture range, and evaluated the incidence of island errors in the dataset.

We observed that no errors are encountered with an obscuration of 60% of a metapixel, whereas almost half of the dataset is affected by wrong reconstruction with 80% shadowing. The percentage of bad frames depends also on the mutual orientation of the spider, fringes of tilt, and pixel grid. We then observed that a better resolution yields in general lower error counts due to a finer discretization of the spider shadow on the pixel grid and fewer obscured metapixels. Finally, we argued that a relevant trigger for island errors is the pixel-scale artefacts at the edge of the shadows and that is possible to reduce their impact with a proper selection of the modulation threshold.

In the end, we identified the most favorable opto-mechanical setup and interferometer settings to reduce the incidence of island error to a minimum and summarized these findings in a laboratory checklist.

6 Appendix A: Laboratory Procedures

6.1 How to Inspect the Test Setup

We report here a procedure for the direct testing of the optical setup for island errors. If the interferometer software features a free run or continuous mode, i.e., the WF map is computed continuously on the fly, such a mode should be activated to speed up the process. Alternatively, the user should collect and inspect a sample of frames when requested.

1. Evaluate the actual pixel-scale in your setup and compare it with the spider thickness; consider the option of changing the pixel-scale or the spider thickness.
2. Draw the detector mask to define the illuminated pupil, without masking the spider.
3. Disable any bridging option in the software.
4. Align the setup to zero WF tilt.
5. Adjust the beam ratio, exposure, and camera gain to optimize the contrast.
6. Set both the modulation and intensity threshold to 0.
7. Collect WF frames (in countinuous mode) while increasing the alignment tilt horizontally, vertically, and diagonally.
8. Identify the WF tilt (PtV) when island errors start occurring; consider this value as a limit during your measurements.

9. Increase the alignment tilt until a significant fraction of the frames is affected by errors; run the rest of this checklist in this regime.
10. Identify the reconstruction direction of the phase-unwrapping algorithm as the direction of fringes of tilt when no island errors are detected even in large tilt regime.
11. If possible, rotate your setup to have the spider parallel to the reconstruction direction.
12. If it is possible to select the kernel of the reconstruction algorithm, try testing the 2×2 and 3×3 options and check which kernel yields the lower error incidence.
13. If the software allows for the selection of different reconstruction algorithms and/or reconstruction options, try testing them and check which works best; in general, parallel or speed-optimized options yield poorer results.
14. If the test facility is affected by significant vibration or acoustic noise, try reducing the exposure time to a minimum to minimize the signal loss due to fringe smearing.
15. Try (if allowed by the optical layout) to defocus the spider on the detector and check if a lower error incidence is observed.

Without reducing the alignment tilt, start the procedure for the tuning of the modulation threshold.

6.2 How to Adjust the Modulation Threshold

The modulation threshold should be tuned with the optical alignment adjusted to have a significant amount of fringes of tilt in the WF, to be conservative versus a worst case scenario. As a rule of the thumb, consider a slope comparable to half of the capture range over the spider shadow. In general, interferometer software allows for the real time visualization of the modulation index,

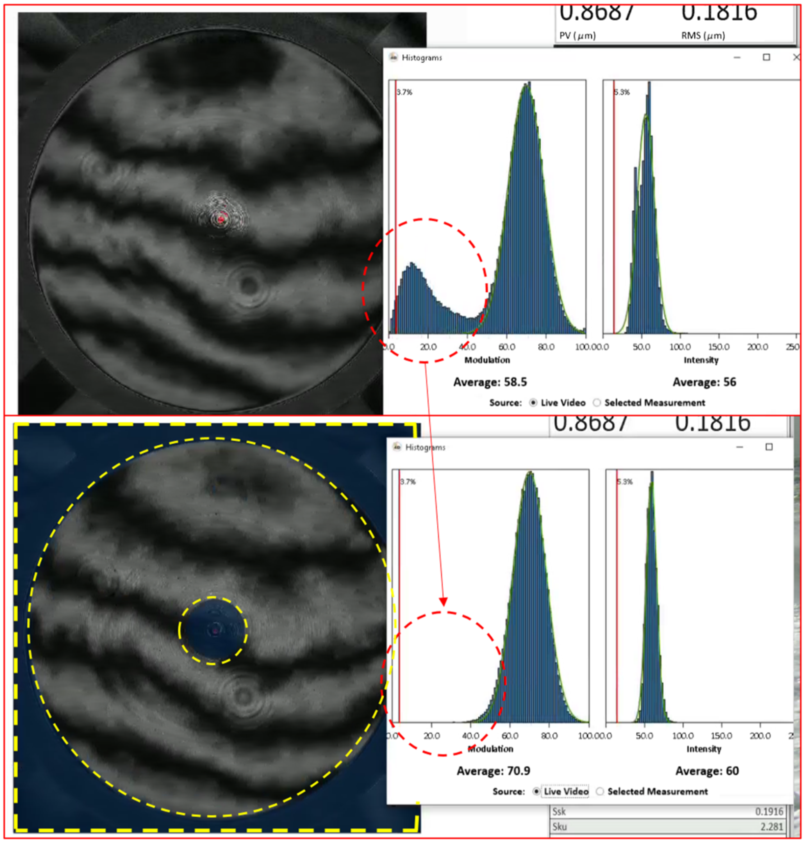

Fig. 8 Interferometric image together with modulation and intensity histogram. The upper red circle indicates the secondary peak in the modulation plot due to non-illuminated pixels, which in this image is outside the circular pupil. In the lower panel, the outer part of the frame was masked (region within the yellow dashed lines). Pixels below the spiders have a typically low modulation index and produce a secondary peak in the modulation plot similar to this one.

see for instance the histograms presented in Fig. 8 for reference. As a first step, define the detector mask to get rid of those pixels that are outside the measurement area. The distribution of the modulation values with and without the detector mask is shown in Fig. 8 to clarify the effect of non-illuminated pixels. Do not mask pixels below the spider because the interferometer SW will automatically divide the measurement area into separated islands. The tuning of the modulation threshold is summarized in the following procedure.

1. Roughly adjust the fringe contrast by tuning the ratio test beam versus reference beam, until the black fringe level is set to a minimum; then, adjust the exposure time or camera gain to raise the white fringe level.
2. Fine-tune the ratio of the reference beam versus the test beam to have a modulation histogram peak at the right side of the plot (i.e., peak at 70% to 80%), as shown in Fig. 9.
3. Identify on the plot the pixel below the spider as those with low modulation index; refer to Fig. 8, where small peak on the left in the modulation histogram is due to the pixel in the masked area. Consider that the total number of pixels below the spider may be very low, so the peak at low modulation may have a very small amplitude.
4. Change the modulation threshold to values lower than, equal to, and larger than the secondary peak, and test in these cases the effect on the reconstructed images in terms of island errors.

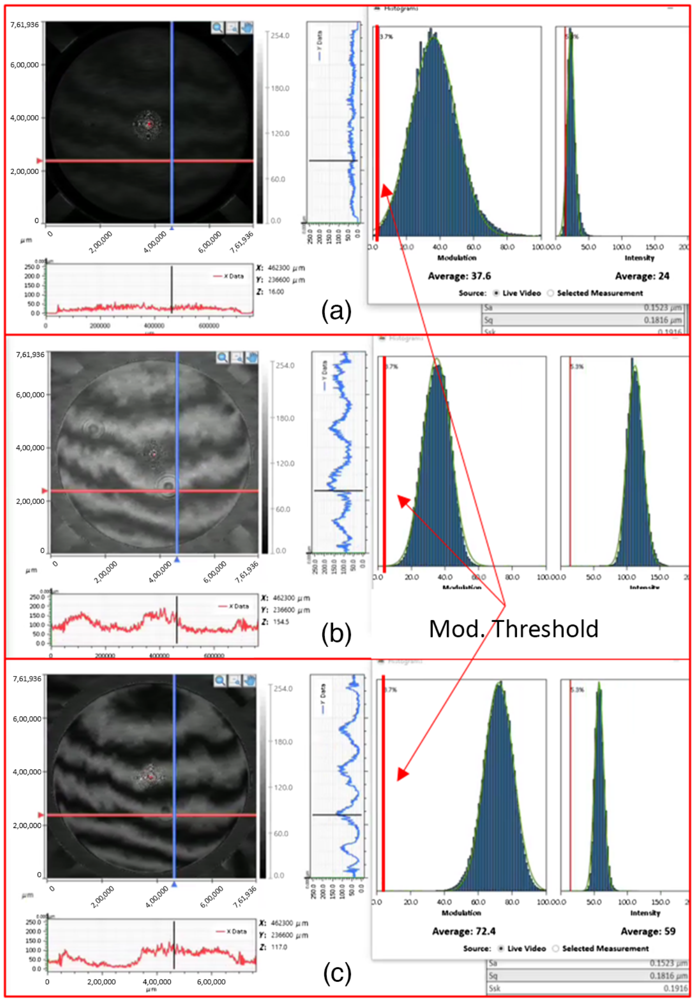

Fig. 9 Three modulation histograms corresponding to different illumination and contrast conditions on the optical setup. (a) The very marginal sampling conditions, to be avoided; (b) the acceptable conditions for most of the testing scenarios; however, compared with (c), a much smaller range of modulation values is available for selecting a proper threshold; (c) is definitively a best case.

5. If the secondary peak is not visible, or if it is not due to the pixel below the spider, set the modulation threshold to 0% and then increase it in steps of 5% (e.g.,) while checking the occurrence of island errors.

7 Appendix B: Description of the Algorithms Tested on the DSM

7.1 Islands Errors and Images Selection

A possible approach for the DM calibration procedure consists of selecting only those frames that are not affected by island errors and discarding all others. Such an approach was not taken into account as a baseline for the calibration of the DSM. In fact, the calibration procedure implements a large degree of automation and synchronization among the interferometer, DM, alignment devices, data storage, and processing workstations, together with the production of a large amount of associated metadata. The complete dataset is required to produce a calibration step, so it would be very impractical to identify, remove, and re-acquire those single bad frames within a dataset. The approach may, however, be adopted when running a simpler measurement procedure.

7.2 Islands Leveling: Gap Bridging

The algorithm is based on the measurement of the vertical gap measured at the inter-island boundary. The procedure may be summarized as follows:

1. the image and its valid points mask are loaded;
2. the islands are identified within the mask;
3. a number (e.g., 4) of azimuthal profiles are drawn on the image, and the associated pixels are extracted;
4. a polynomial function is fitted of the (e.g.,) 20 pixels before and after the gap, and the vertical offset is measured by extrapolating the functions across the gap;
5. the values found are trimmed to integer values of λ and then applied to the associated islands.

Such a procedure was adopted in particular for the correction of absolute images,[16] i.e., those frames representing the current mirror shape. The WF content of these images includes the air convection, the aberration from the alignment residue, and the high orders from the DM flattening residue (partial actuator correction). Such contributors affect the procedure because the very local features from air convection and partial flattening could be larger than $\lambda/2$. To this purpose, time averaging could help to reduce the local contribution from convection, and measuring the profile on several radial distances could reduce the impact of the DM features. In Fig. 10, we show a typical absolute image of the DSM with one associated azimuthal profile. The figure shows clearly how the local features are entangled with the island error as measured on the gaps.

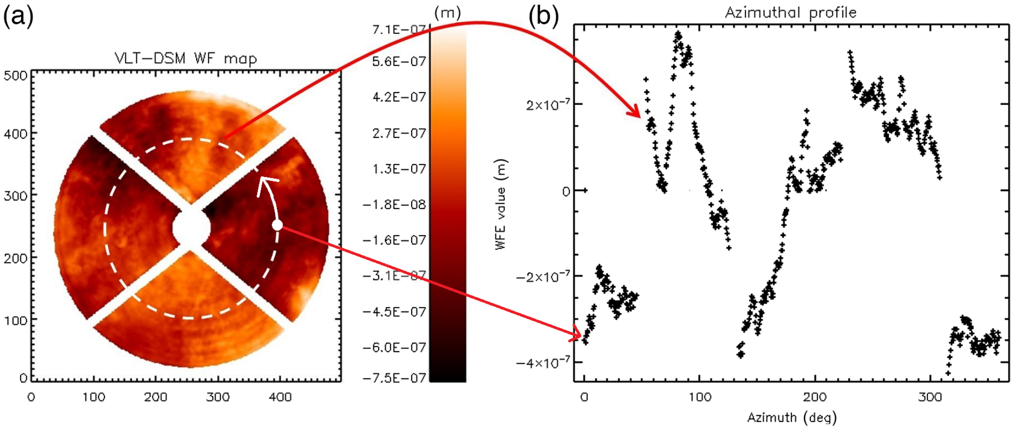

Fig. 10 Example of the gap-bridging algorithm: (a) an azimuthal profile is extracted from the phase map and (b) the points below the spider shadow are extrapolated to correct the island error. In this specific case, the right hand island is affected by a $-\lambda$ error.

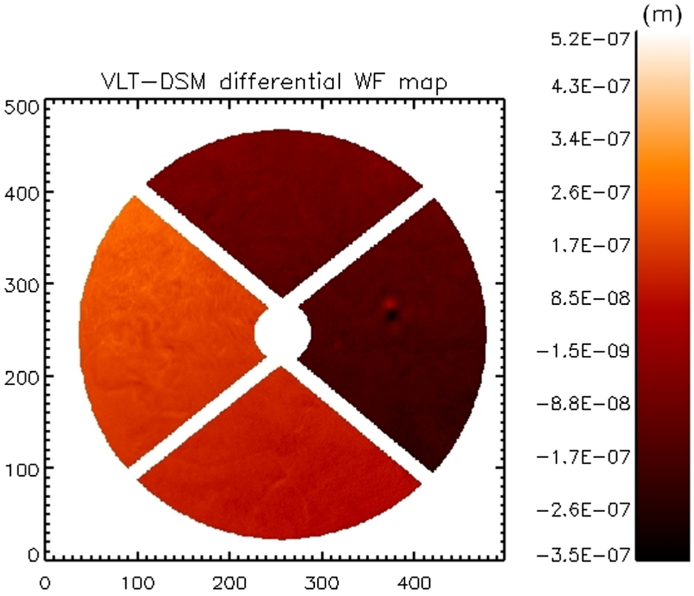

Fig. 11 Push-pull (differential) WF map with an actuator poked (right sector).

7.3 Islands Leveling: Mixed Islands and Actuators IF

When dealing with differential imaging, some *a-priori* information may be used to correct the island errors. Differential imaging refers to the measurement of two consecutive frames at a high cadence while a differential command is applied to the DM; for instance, it is used to measure the actuators IFs with the push-pull technique. In a differential image, the static features (such as the mirror aberration) and slow drift as convection are nulled or greatly reduced, and the result is an almost flat phase map (within 5 to 10 nm RMS pixel-scale noise) plus the shape corresponding to the command applied. In Fig. 11, a typical DSM WF map is shown; on the right island, the signal of a poked actuator is visible. Because the print-through of such a command is known, it may be fitted on the image using a projection matrix, which includes the signal associated with the individual island piston. The procedure is as follows:

1. two consecutive frames are loaded along with their measurement masks, and the frames difference ω and mask intersection are computed;
2. the islands are identified on the mask;
3. the differential actuator command applied on the frames is restored;
4. the command is fitted using thin plate splines to create a sythetic WF map ω_c associated with it; a previous record of IF cannot be used because it might be affected by island errors;
5. a five vectors modal basis M is created with the synthetic map and the four differential piston maps: $M = [\omega_c; \pi_0; \pi_1; \pi_2; \pi_3]$; the basis is pseudo-inverted to create a projection matrix $R = M^{-1}$;
6. the image ω is corrected as $\omega_1 = M_{\mathrm{isl}} R \omega$, where M_{isl} is the submatrix including only the island piston signal.

Such a computation allows for separating the intrinsic command contribution to the island mean value from that of the island error, which in turn is fitted well within the required accuracy of $\lambda/2$.

The algorithm was run on all IFs and actuator calibration images with very good results.

7.4 Vignetted Actuators Selection and Dedicated Control

The actuators below the spider shadow may suffer from partial or even total lack of interferometer signal, so it is not possible to drive them in an optical closed loop. In Fig. 12, we show a DSM WF map together with the actuator locations. The spider shadow in the image is actually sligthly larger than the effective one due to post-processing options (e.g., automatic trimming of edge pixels); however, it is evident that a large number of actuators have their area of interest

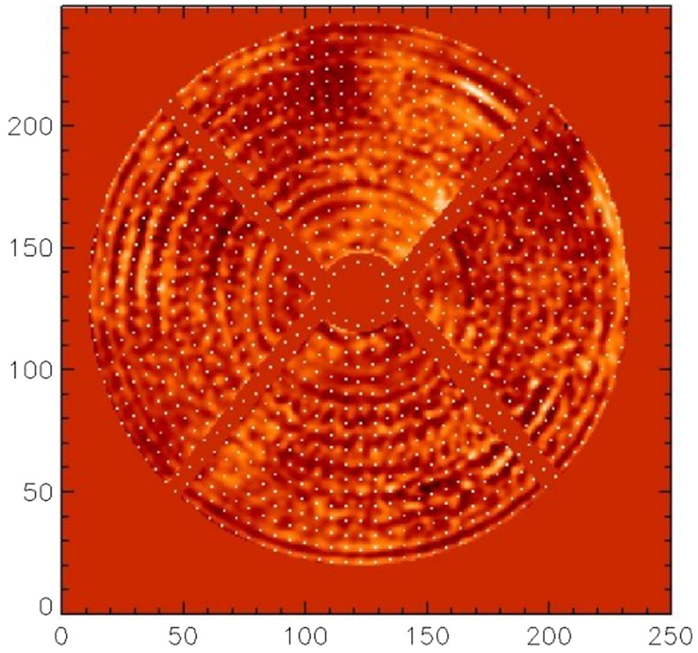

Fig. 12 Locations of the DSM actuators in the phase map to show those falling below the spider shadow.

completely within the shadow. This is consistent with the effective shadowing of 32 mm and the actuator pitch of ≈30 mm. A precise method for the identification of vignetted actuators is based on the measurement of the IF and their selection according to a given signal threshold, for instance 20% of the averaged signal RMS of the visible actuator. According to such a procedure, we identified 114 actuators masked by the spider and defined for them a special control strategy named slaving. Our strategy was specifically tailored for the DSM voice-coil actuators controlled with an internal metrology based on capacitive sensors. The starting point is the definition of a mirror modes matrix V and the associated stiffness matrix K, such as $F = KV$; the procedure consists of the computation of a new V' matrix, which satisfy the condition $F_p = 0$, where p is the list of the vignetted actuators. The V' matrix has by definition a lower number of modes (columns) but is defined over the entire set of actuators (rows). Accordingly, a new K' stiffness matrix is obtained. Different types of actuators may be slaved according to different procedures. For instance, their command may be retrieved by interpolating the neighboring actuator ones.

Acknowledgment

The authors declare no competing interests in the manuscript and no other potential conflicts of interest to disclose.

References

1. J. Harvey and C. Ftaclas, "Diffraction effects of telescope secondary mirror spiders on various image-quality criteria," *Appl. Opt.* **34**, 6337–49 (1995).
2. A. Obereder, S. Raffetseder, and V. A. Hutterer, "Dealing with spiders on ELTs: using a Pyramid WFS to overcome residual piston effects," *Proc. SPIE* **10703**, 107031D (2018).
3. J.-F. Sauvage et al., "Tackling down the low wind effect on SPHERE instrument," *Proc. SPIE* **9909**, 990916 (2016).
4. S. Bonnefond et al., "Wavefront reconstruction with pupil fragmentation: study of a simple case," *Proc. SPIE* **9909**, 990972 (2016).
5. E. Pinna et al., "Design and numerical simulations of the GMT natural guide star WFS," *Proc. SPIE* **9148**, 91482M (2014).
6. S. Esposito et al., "Laboratory characterization and performance of the high-order adaptive optics system for the Large Binocular Telescope," *Appl. Opt.* **49**, G174 (2010).

7. L. M. Close et al., "First closed-loop visible AO test results for the advanced adaptive secondary AO system for the Magellan Telescope: MagAO's performance and status," *Proc. SPIE* **8447**, 84470X (2012).
8. A. Riccardi et al., "The adaptive secondary mirror for the Large Binocular Telescope: optical acceptance test and preliminary on-sky commissioning results," *Proc. SPIE* **7736**, 77362C (2010).
9. R. Briguglio, F. Quirós-Pacheco, and J. A. Males, "Optical calibration and performance of the adaptive secondary mirror at the Magellan telescope," *Sci. Rep.* **8**, 10835 (2018).
10. R. Briguglio et al., "The deformable secondary mirror of VLT: final electro-mechanical and optical acceptance test results," *Proc. SPIE* **9148**, 914845 (2014).
11. R. Stuik et al., "Deploying the testbed for the VLT adaptive optics facility: ASSIST," *Proc. SPIE* **8447**, 84473A (2012).
12. G. Pariani et al., "Optical calibration of the ELT adaptive mirror M4: design, alignment and verification of the interferometric test tower," in *Proc. Fifth AO4ELT Conf.* (2017).
13. J. E. Millerd et al., "Pixelated phase-mask dynamic interferometer," *Proc. SPIE* **5531**, 304–314 (2004).
14. N. Brock et al., "Dynamic interferometry," *Proc. SPIE* **5875**, 101–110 (2005).
15. J. E. Millerd and M. North-Morris, "Dynamic interferometry: measurement of space optics and structures," *Proc. SPIE* **10329**, 103291G (2017).
16. R. Briguglio et al., "Optical calibration and test of the VLT Deformable Secondary Mirror," in *Proc. Third AO4ELT Conf.*, S. Esposito and L. Fini, eds., p. 105 (2013).

Runa Briguglio is a researcher at Istituto Nazionale di Astrofisica (INAF)—Arcetri Observatory and is a member of Adaptive Optics National Laboratory in Italy (ADONI). He has been working in the development, calibration, and telescope commissioning of the deformable secondary mirrors (DSMs) for the Large Binocular Telescope (LBT), the Magellan telescope and the Very Large Telescope (VLT) and other instrument projects related to adaptive optics. He is currently working on the preparation of the optical calibration of the European Extremely Large Telescope (ELT) adaptive mirror M4.

Giorgio Pariani is a researcher at INAF—Merate Observatory and is a member of ADONI. He has been working in the development, calibration, and telescope commissioning of the DSMs for LBT, Magellan, and VLT and other instrument projects related to adaptive optics. He is currently working on the preparation of the optical calibration of the ELT adaptive mirror M4.

Marco Xompero is a researcher at INAF—Arcetri Observatory and is a member of ADONI. He has been working in the development, calibration, and telescope commissioning of the DSMs for LBT, Magellan, and VLT and other instrument projects related to adaptive optics. He is currently working on the preparation of the optical calibration of the ELT adaptive mirror M4.

Nicolò Azzaroli is a non-permanent staff member in the Adaptive Optics Group at INAF—Arcetri Observatory and Merate Observatory. He made a significant contribution to the work by preparing the analysis software and running the data processing.

Chiara Selmi is a non-permanent staff member in the Adaptive Optics Group at INAF—Arcetri Observatory and Merate Observatory. She made a significant contribution to the work by preparing the analysis software and running the data processing.

Armando Riccardi is a researcher at INAF—Arcetri Observatory and is a member of ADONI. He has been working in the development, calibration, and telescope commissioning of the DSMs for LBT, Magellan, and VLT and other instrument projects related to adaptive optics. He is currently working on the preparation of the optical calibration of the ELT adaptive mirror M4.

Luca Oggioni is a non-permanent staff member in the Adaptive Optics Group at INAF—Arcetri Observatory and Merate Observatory. He made a significant contribution to the work by preparing the analysis software and running the data processing.